Global Time-Delay Estimation in Ultrasound Elastography

Hoda S. Hashemi and Hassan Rivaz

Among Editor's Selection of Articles in TUFFC in 2017, Dec 2018

***Abstract*—A critical step in quasi-static ultrasound elastography is estimation of time-delay between two frames of radio-frequency (RF) data that are obtained while the tissue is undergoing deformation. This paper presents a novel technique for time-delay estimation (TDE) of *all samples of RF data simultaneously*, thereby exploiting all the information in RF data for TDE. A nonlinear cost function that incorporates similarity of RF data intensity and prior information of displacement continuity is formulated. Optimization of this function involves searching for TDE of all samples of the RF data, rendering the optimization intractable with conventional techniques given that the number of variables can be approximately one million. Therefore, the optimization problem is converted to a sparse linear system of equations, and is solved in real-time using a computationally efficient optimization technique. We call our method GLUE (GLobal Ultrasound Elastography), and compare it to Dynamic Programming Analytic Minimization (DPAM) [1] and Normalized Cross Correlation (NCC) techniques. Our simulation results show that the Contrast to Noise Ratio (CNR) values of the axial strain maps are 4.94 for NCC, 14.62 for DPAM, and 26.31 for GLUE. Our results on experimental data from tissue mimicking phantoms show that CNR values of the axial strain maps are 1.07 for NCC, 16.01 for DPAM, and 18.21 for GLUE. Finally, our results on *in-vivo* data shows that CNR values of the axial strain maps are 3.56 for DPAM and 13.20 for GLUE.**

***Index Terms*—Quasi-static elastography, Real-time elastography, Ultrasound, Time-delay estimation, TDE, Regularized elastography**

I. Introduction

Ultrasound elastography reveals viscoelastic properties of tissue, which are often correlated with pathology, and is therefore of significant clinical importance. Elastography has evolved into several different techniques, but it can broadly be grouped into dynamic and quasi-static elastography [2]–[7]. Dynamic elastography techniques include shear wave imaging [8] and acoustic radiation force imaging [9], which generate deformation in the tissue using ultrasound and provide quantitative mechanical properties of tissue. This work focuses on quasi-static elastography, and more particularly on free-hand palpation elastography, wherein tissue deformation is slow and is generated by slowly palpating the tissue with the hand-held ultrasound probe.

Free-hand elastography and shear wave elastography each has its own strengths. Free-hand strain imaging does not provide quantitative elasticity measures, unless it is combined with an inverse problem approach [10]–[14] that solves for tissue elasticity, whereas shear-wave elastography techniques provide quantitative values of tissue elasticity or shear moduli [15]–[17]. An advantage of freehand strain imaging emanates from the larger displacement fields compared to that of shear-wave elastography, which can lead to less noise in the estimated displacement field. Although elastography techniques vary significantly in the way they generate tissue deformation and in the biomechanical property they investigate, they all require estimation of tissue displacement, commonly referred to as Time-Delay Estimation (TDE) using ultrasound radio-frequency (RF) signal. TDE is challenging and an active field of research due to various sources of noise and signal decorrelation. In this paper, we focus on TDE in freehand palpation elastography [18]–[23]. This approach is attractive as it works with traditional ultrasound machines and does not require any additional hardware.

Window-based techniques calculate TDE for small windows (segments) of the RF data, and can be categorized into amplitude- and phased-based. Amplitude-based methods maximize cross correlation or normalized cross correlation (NCC) [24]–[27], whereas phase-based methods find the zero-crossing of the phase of the cross correlation [28]–[33]. Window-based displacement estimation techniques can also be categorized by the dimensionality of the search range: 1D methods only search in axial directions [18], [34], [35], and 2D techniques perform a search in both axial and lateral directions [36]–[39]. Since the underlying displacement field is usually 3D, 2D displacement estimation techniques generally outperform their 1D counterparts. The importance of 2D displacement estimation is twofold: it provides more accurate estimates of axial strain [40], and it can be used for reconstruction of tissue elastic properties [10]–[14]. One of the disadvantages of window-based methods is their sensitivity to signal decorrelation, which can be caused by small out-of-plane motion of the probe or large deformations. Larger windows, approximately of the size 10 ultrasound wavelengths or larger [41], [42], provide more information and hence reduce the estimation variance, but they result in significant signal decorrelation and also decrease the spatial resolution. Remedies for these problems have been proposed such as warping the data [43]–[45], which are generally computationally expensive.

An attractive alternative approach to correlation-based methods is minimization of a regularized cost function [3], [46]–[50]. These methods exploit the prior information that tissue deformation is smooth, and therefore are robust to signal decorrelation. A disadvantage of these methods is their computational complexity, and as such, they are not readily suitable for real-time implementation. We proposed a real-time technique for estimating fine subpixel tissue displacement

H. S. Hashemi and H. Rivaz are with the Department of Electrical and Computer Engineering and the PERFORM Centre, Concordia University, Montreal, QC, H3G 1M8, Canada

Email: ho_hash@ece.concordia.ca and hrivaz@ece.concordia.ca

Manuscript received —-; revised —.

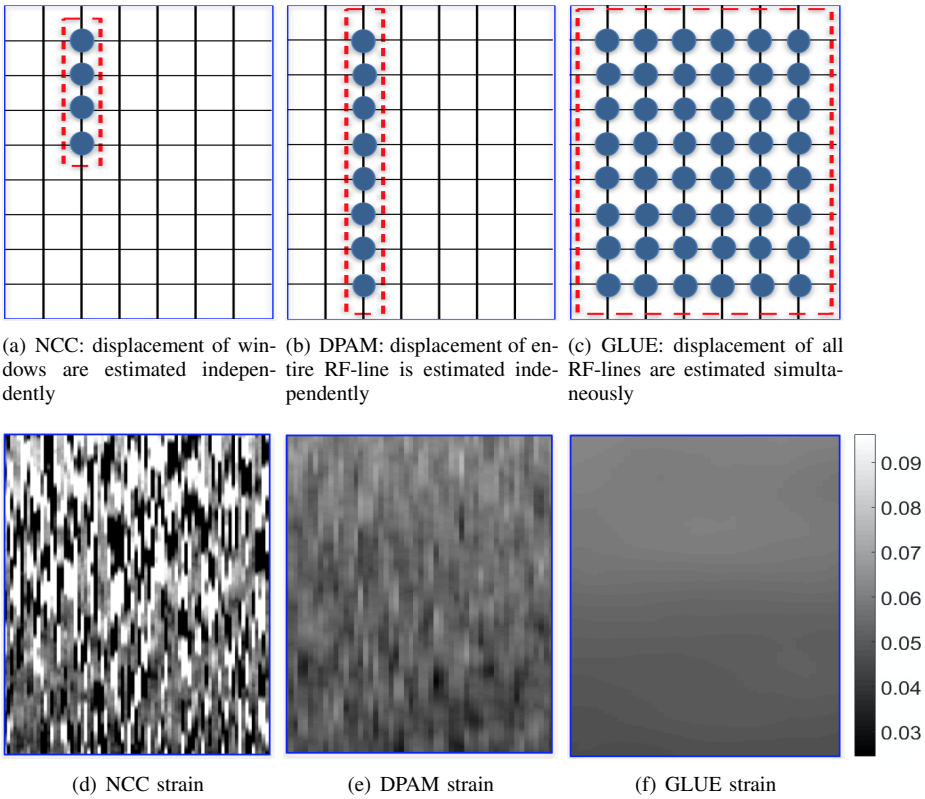

(a) NCC: displacement of windows are estimated independently

(b) DPAM: displacement of entire RF-line is estimated independently

(c) GLUE: displacement of all RF-lines are estimated simultaneously

(d) NCC strain

(e) DPAM strain

(f) GLUE strain

Fig. 1. Comparison of NCC, DPAM and GLUE algorithms, with the corresponding strain images in the second row. In (a) to (c), each circle shows an RF sample that is utilized in TDE. Each grid point corresponds to a sample in RF data. Few samples are shown here to ease visualization; real RF data contains significantly more samples. In (a), few samples are grouped together to form a window, which is used to calculate NCC. The displacement of all samples in an entire RF-line in DPAM (b) or the entire image in GLUE (c) are estimated together. (d) to (f) show strain images of a homogeneous phantom. Note that the average strain is 8%. GLUE substantially outperforms both NCC and DPAM by utilizing all data in the RF-frame.

maps using Dynamic Programming and Analytic Minimization (DPAM) of a regularized cost function [1], [51], whereby displacements of all the samples in an RF-line are estimated simultaneously. This simultaneous estimation results in both more robust and accurate displacement estimates compared to NCC-based methods that only utilize data within a window. In [1], the subpixel displacement of a seed-line is calculated first, and is used as an initial estimate for neighboring RF-lines. This algorithm, however, has three drawbacks. First, the simultaneous estimation is limited to individual RF-lines, thereby only utilizing a small fraction of the information available from the entire image. Second, displacement estimates are discontinuous between adjacent RF-lines, creating artifacts in the form of vertical streaks in the strain image. And third, displacement estimation in each line depends on the initial estimate, i.e. the displacement of the previous RF-line. Hence, if there is large decorrelation or noise in an RF-line that results in failure of its displacement estimation, the erroneous displacement propagates to the consequent RF-lines. We present herein a novel method for estimating accurate 2D displacement maps wherein the displacement of the entire image is estimated simultaneously. We call the new method GLobal Ultrasound Elastography (GLUE). Figure 1 provides a schematic comparison of three different methods:

(a) Window-based methods, which calculate the displacements of each correlation window independently typically of the size about 50 samples.

(b) DPAM, which uses the information of an RF-line typically of the size about 1000 samples, to acquire the displacements of all samples of the RF data.

(c) GLUE, which utilizes the information of all image samples typically of the size $1000 \times 100 = 10^5$, and calculates TDE of all the samples of the RF frame simultaneously.

GLUE calculates the axial and lateral displacements of all samples of RF data by minimizing a nonlinear cost function. Therefore, for a typical RF frame of size 1000×100, there are 2×10^5 variables in the cost function. Typical optimization methods can be intractable in terms of both processing and memory requirements. We convert the optimization problem into a system of equations which entails solving a sparse linear system, and as such, is computationally efficient. We show that our method substantially outperforms previous work using simulation, phantom and *in-vivo* liver data. An executable implementation of GLUE can be found at https://users.encs.concordia.ca/~hrivaz/Ultrasound_Elastography/.

The *in-vivo* data in this paper is obtained from patients with liver tumor who underwent radiofrequency (RF) ablation surgery. Qualitative and quantitative imaging techniques for staging of liver diseases have been implemented on ultrasound, computed tomography (CT), and magnetic resonance

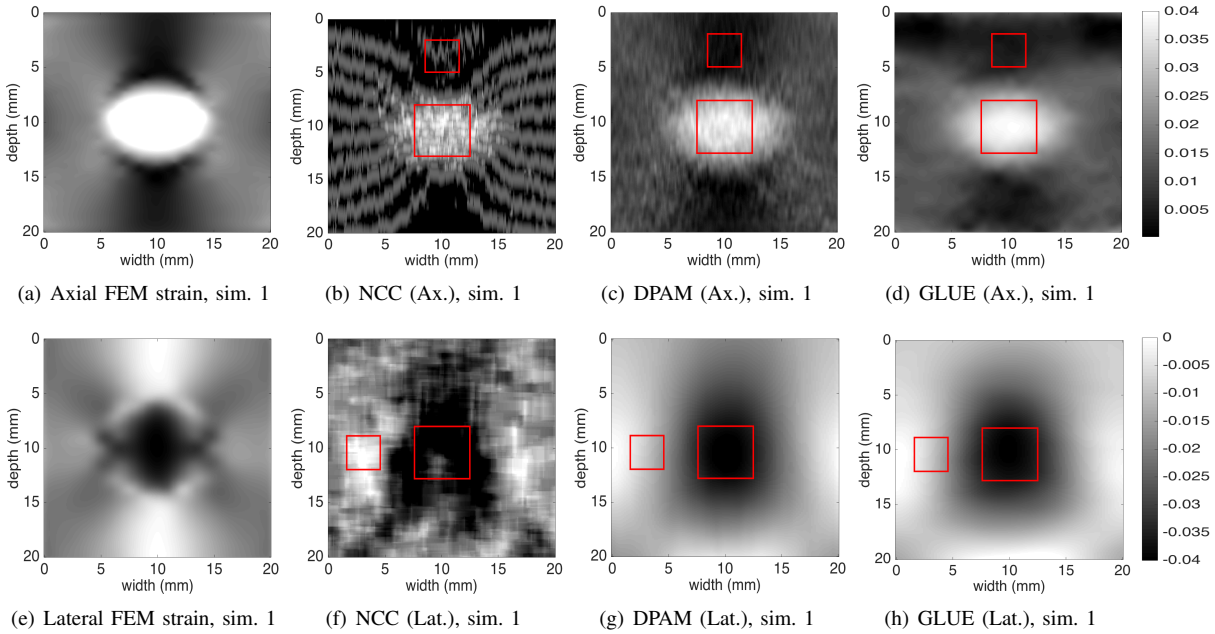

(a) Axial FEM strain, sim. 1 (b) NCC (Ax.), sim. 1 (c) DPAM (Ax.), sim. 1 (d) GLUE (Ax.), sim. 1

(e) Lateral FEM strain, sim. 1 (f) NCC (Lat.), sim. 1 (g) DPAM (Lat.), sim. 1 (h) GLUE (Lat.), sim. 1

Fig. 2. Field II and FEM simulation results. (a) is the axial ground truth strain. (b) to (d) show the axial strain images of the first simulation. (e) is the lateral ground truth strain. (f) to (h) show the lateral strain images of the first simulation. GLUE substantially outperforms NCC and DPAM in all results. Target and background windows used for CNR calculation are shown in red. The SNR is calculated for the background window.

imaging (MRI) scanners to address the limitations of liver biopsy. Among these techniques, ultrasound elastography is the most widely used clinically [52]. Liver stiffness estimated by elastography techniques is used to evaluate the severity of the underlying chronic liver disease, guide treatment decision, assess disease outcome, and evaluate response to therapy [7].

II. Methods

In this section, we first briefly describe the closely related previous work [1]. We then present GLUE, and derive equations that enable us to globally calculate TDE of all samples of the RF data simultaneously.

A. Dynamic Programming Analytic Minimization (DPAM)

Let I_1 and I_2 be images of size $m \times n$ corresponding to before and after some deformation. In DPAM [1], first the initial integer displacement estimates in the axial (a_i) and lateral (l_i) directions are calculated using dynamic programming (DP) for all $i = 1, \cdots, m$ samples of an RF-line, which is called a seed-line. DP only provides integer displacement estimates, which are not accurate enough for elastography. Therefore, by minimizing the following regularized cost function, the sub-sample Δa_i and Δl_i values are calculated such that the duple $(a_i + \Delta a_i, l_i + \Delta l_i)$ gives the axial and lateral displacements at the sample i of the seed-line:

$$\begin{aligned} &C_s(\Delta a_1, \cdots, \Delta a_m, \Delta l_1, \cdots, \Delta l_m,) = \\ &\textstyle\sum_{i=1}^{m}\{[I_1(i,s) - I_2(i + a_i + \Delta a_i, s + l_i + \Delta l_i)]^2 \\ &+\alpha(a_i + \Delta a_i - a_{i-1} - \Delta a_{i-1})^2 \\ &+\beta_a(l_i + \Delta l_i - l_{i-1} - \Delta l_{i-1})^2 \\ &+\beta'_l(l_i + \Delta l_i - l_{i,s-1})^2\} \end{aligned} \tag{1}$$

where s indicates the lateral position of the seed RF-line (i.e. A-line number). The regularization weight α determines how close the axial displacement of each sample should be to its neighbor on the top, and the weights β_a and β'_l determine how close lateral displacement of each sample should be to its neighbors on the top and left. The displacement of the rest of the lines is calculated similar to the seed-line, except that the initial displacements are set to that of the previous line (instead of DP). Since we perform the calculations for one RF-line at a time, we drop the index s to simplify the notations: a_i , l_i , Δa_i and Δl_i are in fact $a_{i,s}$, $l_{i,s}$, $\Delta a_{i,s}$ and $\Delta l_{i,s}$. Using 2D Taylor expansion of the data term in (2) around $(i + a_i, j + l_i)$ gives:

$$I_2(i+a_i+\Delta a_i, j+l_i+\Delta l_i) \approx I_2(i+a_i, j+l_i)+\Delta a_i I'_{2,a}+\Delta l_i I'_{2,l} \tag{2}$$

where $I'_{2,a}$ and $I'_{2,l}$ are the derivatives of the I_2 at point $(i + a_i, j + l_i)$ in the axial and lateral directions respectively. The optimal $(\Delta a_i, \Delta l_i)$ values occur when the partial derivatives of C_s with respect to both Δa_i and Δl_i are zero. Setting $\frac{\partial C_s}{\partial \Delta a_i} = 0$ and $\frac{\partial C_s}{\partial \Delta l_i} = 0$ for $i = 1, \cdots, m$ and stacking the $2m$ unknowns in $\Delta d = [\Delta a_1\ \Delta l_1\ \Delta a_2\ \Delta l_2\ \cdots\ \Delta a_m\ \Delta l_m]^T$ and the $2m$ initial estimates in $d = [a_1\ l_1\ a_2\ l_2 \cdots\ a_m\ l_m]^T$ [1]:

$$A\Delta d = b, \tag{3}$$

where A is a coefficient matrix of size $2m \times 2m$, and b is a vector of length $2m$. An important characteristic of A is that it is penta-diagonal. Therefore, we used the Thomas algorithm [53] in DPAM to efficiently optimize Eq 3. In summary, solving Eq. 3 provides TDE for all samples of an RF-line, and for each A-line, this equation is solved independently. We now propose GLUE, a new technique that provides TDE of all RF samples within an image.

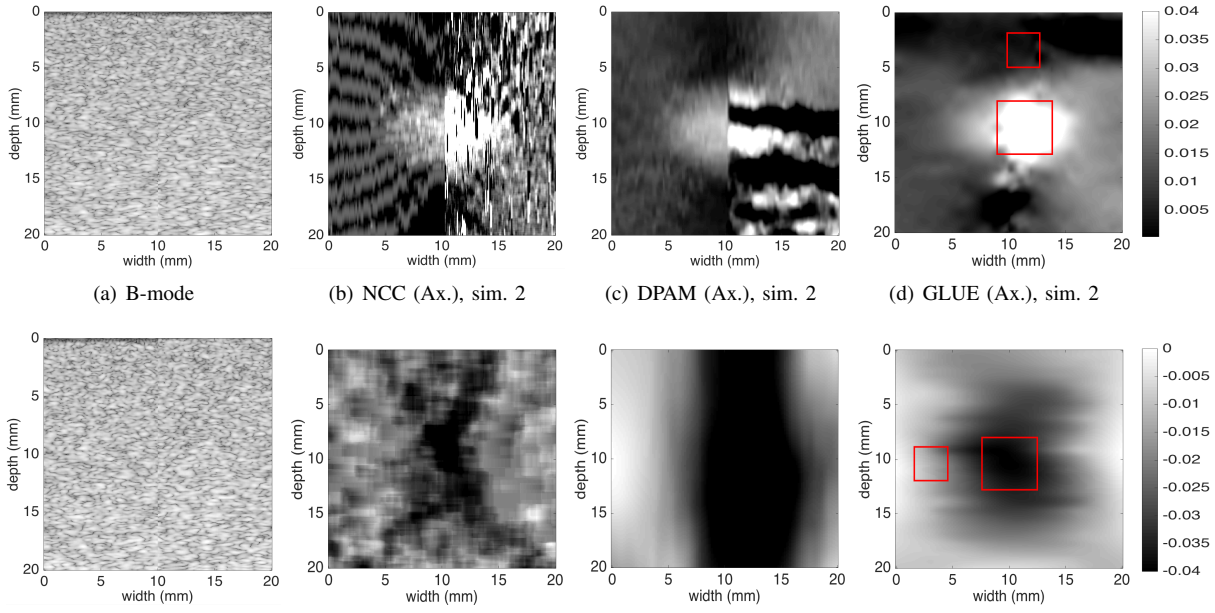

(a) B-mode (b) NCC (Ax.), sim. 2 (c) DPAM (Ax.), sim. 2 (d) GLUE (Ax.), sim. 2

(e) B-mode (f) NCC (Lat.), sim. 2 (g) DPAM (Lat.), sim. 2 (h) GLUE (Lat.), sim. 2

Fig. 3. Field II and FEM simulation results. A vertical slippage exists in the motion field at the middle of the image. (a) is the first ultrasound image. (b) to (d) are the axial strain images. (e) is the second ultrasound image. (f) to (h) are the lateral strain images. Target and background windows used for CNR calculation of the GLUE results are shown in red. The SNR is calculated for the background window.

B. Global Time-Delay Estimation (GLUE)

Similar to DPAM, GLUE calculates TDE by optimization of a cost function that incorporates both amplitude similarity and displacement continuity. The difference is that GLUE cost function is formulated for the entire image instead of a single RF-line. In GLUE, we use Taylor expansion similar to DPAM to arrive at a linear system of equations similar to Eq. 3. However, as we will elaborate, the coefficient matrix will not become penta-diagonal, and therefore, the linear system of equations cannot be efficiently solved using traditional methods such as the Thomas algorithm [53]. We will therefore borrow an efficient optimization method from the big data field. The outline of our proposed technique is as follows:

1) Estimation of integer displacements using DP [49].
2) Refinement of DP estimates using GLUE.
3) Strain estimation by spatially differentiating the displacement field.

We now elaborate the second step, which is the main contribution of this work. Let DP initial estimates be $a_{i,j}$ and $l_{i,j}$. Our cost function is

$$\begin{aligned}&C(\Delta a_{1,1},\cdots,\Delta a_{m,n},\Delta l_{1,1},\cdots,\Delta l_{m,n})=\\&\textstyle\sum_{j=1}^{n}\sum_{i=1}^{m}\{[I_1(i,j)-I_2(i+a_{i,j}+\Delta a_{i,j},j+l_{i,j}+\Delta l_{i,j})]^2\\&+\alpha_1(a_{i,j}+\Delta a_{i,j}-a_{i-1,j}-\Delta a_{i-1,j})^2\\&+\beta_1(l_{i,j}+\Delta l_{i,j}-l_{i-1,j}-\Delta l_{i-1,j})^2\\&+\alpha_2(a_{i,j}+\Delta a_{i,j}-a_{i,j-1}-\Delta a_{i,j-1})^2\\&+\beta_2(l_{i,j}+\Delta l_{i,j}-l_{i,j-1}-\Delta l_{i,j-1})^2\}\end{aligned}\tag{4}$$

where α and β are regularization terms for axial and lateral displacements respectively. Note that this function has mn variables of $\Delta a_{i,j}$ and mn variables of $\Delta l_{i,j}$, resulting a total of $2mn$ variables. The first difference between this equation and Eq. 1 is that here, data in all samples are exploited to in the right hand side (note two summations here over m and n, compared to one summation in Eq. 1 over only m). The second difference is that the left hand side has $2mn$ variables, compared to $2m$ in Eq. 1. In other words, all samples of the RF data are utilized in the cost function, and the displacement of all samples are calculated simultaneously.

Using 2D Taylor expansion around $(i+a_{i,j},j+l_{i,j})$, we have

$$\begin{aligned}&C(\Delta a_{1,1},\cdots,\Delta a_{m,n},\Delta l_{1,1},\cdots,\Delta l_{m,n})=\\&\textstyle\sum_{j=1}^{n}\sum_{i=1}^{m}\{[I_1(i,j)-I_2(i+a_{i,j},j+l_{i,j})\\&-\Delta a_{i,j}I'_{2,a}-\Delta l_{i,j}I'_{2,l}]^2\\&+\alpha_1(a_{i,j}+\Delta a_{i,j}-a_{i-1,j}-\Delta a_{i-1,j})^2\\&+\beta_1(l_{i,j}+\Delta l_{i,j}-l_{i-1,j}-\Delta l_{i-1,j})^2\\&+\alpha_2(a_{i,j}+\Delta a_{i,j}-a_{i,j-1}-\Delta a_{i,j-1})^2\\&+\beta_2(l_{i,j}+\Delta l_{i,j}-l_{i,j-1}-\Delta l_{i,j-1})^2\}.\end{aligned}\tag{5}$$

Since $a_{i,j}$ and $l_{i,j}$ are not integer, interpolation is required to calculate $I'_{2,a}$ and $I'_{2,l}$ at the point $(i+a_{i,j},j+l_{i,j})$. Setting $\frac{\partial C_{i,j}}{\partial \Delta a_{i,j}}=0$ and $\frac{\partial C_{i,j}}{\partial \Delta l_{i,j}}=0$ for $i=1,\cdots,m$, $j=1,\cdots,n$, and stacking the $2mn$ unknowns in $\Delta\mathbf{d}=[\Delta a_{1,1}\ \Delta l_{1,1}\ \Delta a_{1,2}\ \Delta l_{1,2}\cdots\Delta a_{1,n}\ \Delta l_{1,n}\ \Delta a_{2,1}\ \Delta l_{2,1}\ \Delta a_{2,2}\ \Delta l_{2,2}\cdots\Delta a_{m,n}\ \Delta l_{m,n}]^T$, and the $2mn$ initial estimates in $\mathbf{d}=[a_{1,1},\ l_{1,1},\ a_{1,2},\ l_{1,2},\ \ldots,\ a_{m,n},\ l_{m,n}]^T$, we have:

$$(H+D)\Delta d=H^*\mu-Dd,\tag{6}$$

where

$$D=\begin{bmatrix}Q&R&O&O&\ldots&O\\R&S&R&O&\ldots&O\\O&R&S&R&\ldots&O\\\vdots&&\ddots&\ddots&\ddots&\\O&O&\ldots&R&S&R\\O&O&\ldots&O&R&Q\end{bmatrix},\tag{7}$$

$$Q = \begin{bmatrix} \alpha_1+\alpha_2 & 0 & -\alpha_2 & 0 & 0 & \dots & 0 \\ 0 & \beta_1+\beta_2 & 0 & -\beta_2 & 0 & \dots & 0 \\ -\alpha_2 & 0 & \alpha_1+2\alpha_2 & 0 & -\alpha_2 & \dots & 0 \\ 0 & -\beta_2 & 0 & \beta_1+2\beta_2 & 0 & \dots & 0 \\ 0 & 0 & -\alpha_2 & 0 & \alpha_1+2\alpha_2 & \dots & 0 \\ \vdots & & & & & \ddots & \\ 0 & 0 & 0 & \dots & & \alpha_1+\alpha_2 & 0 \\ 0 & 0 & 0 & \dots & & 0 & \beta_1+\beta_2 \end{bmatrix}, \tag{8}$$

$$S = \begin{bmatrix} 2\alpha_1+\alpha_2 & 0 & -\alpha_2 & 0 & 0 & \dots & 0 \\ 0 & 2\beta_1+\beta_2 & 0 & -\beta_2 & 0 & \dots & 0 \\ -\alpha_2 & 0 & 2\alpha_1+2\alpha_2 & 0 & -\alpha_2 & \dots & 0 \\ 0 & -\beta_2 & 0 & 2\beta_1+2\beta_2 & 0 & \dots & 0 \\ 0 & 0 & -\alpha_2 & 0 & 2\alpha_1+2\alpha_2 & \dots & 0 \\ \vdots & & & & & \ddots & \\ 0 & 0 & 0 & \dots & & 2\alpha_1+\alpha_2 & 0 \\ 0 & 0 & 0 & \dots & & 0 & 2\beta_1+\beta_2 \end{bmatrix}. \tag{9}$$

Q is a pentadiagonal matrix of size $2n \times 2n$, and O is a zero matrix of size $2n \times 2n$ and

$$R = diag(-\alpha_1, -\beta_1, -\alpha_1, -\beta_1, \dots, -\alpha_1, -\beta_1). \tag{10}$$

where $H = diag(h'^2(1) \ \dots \ h'^2(m))$ is a symmetric tridiagonal matrix with

$$h'^2(i) = \begin{bmatrix} {I'_{2,a}}^2 & I'_{2,a}I'_{2,l} \\ I'_{2,a}I'_{2,l} & {I'_{2,l}}^2 \end{bmatrix} \tag{11}$$

blocks on its diagonal entries where $I'_{2,a}$ and $I'_{2,l}$ are the derivatives of the I_2 at the point $(i + a_{i,j}, j + l_{i,j})$ in the axial and lateral directions, and

$H^* = diag(I'_{2,a}(1,1), I'_{2,l}(1,1), I'_{2,a}(1,2), I'_{2,l}(1,2), \dots, I'_{2,a}(m,n), I'_{2,l}(m,n))$

and

$$\mu = [g_{1,1},\ g_{1,1},\ g_{1,2},\ g_{1,2},\ \dots,\ g_{m,n}]^T, \tag{12}$$

$$g_{i,j} = I_1(i,j) - I_2(i + a_{i,j}, j + l_{i,j}). \tag{13}$$

It is important to note that the coefficient matrix in the left hand side of Eq. 6 is a large matrix of size $2mn \times 2mn$. For a typical RF frame of size 1000×100, this amounts to a matrix of size $200,000 \times 200,000$, which requires 320 GB of memory for storage in double precision floating point format, significantly more than 8 GB that is available in a typical machine. Fortunately, this is a band matrix wherein nonzero elements are confined within a diagonal band of length $4n+1$, thereby significantly reducing the memory requirement. It is important to compare the size of the diagonal bands in the coefficient matrices of Eq. 3 and 6: 5 for DPAM and $4n + 1$ for GLUE. Hence, it is computationally too demanding to use the Thomas algorithm [53] as we did in DPAM to solve Eq. 6. Instead, we use the successive over-relaxation (SOR) method [54], an iterative algorithm for solving linear systems of equations. SOR is significantly faster than traditional methods especially for systems with many variables. It has been applied to various computationally expensive problems such as low-rank factorization [55], support vector machines [56] and computational vision [57].

Once the displacement field is estimated, it is common to estimate its spatial gradient to generate strain images. We consider several displacement measurements and perform a least square regression to calculate the strain image. The smoothness of the strain is obtained from the analytic formulation of the cost function which incorporates the displacement continuity in axial and lateral directions, and the regularization coefficients make it possible to adjust the smoothness to the desired level.

III. Results

In this section, we present results of simulation, phantom and *in-vivo* experiments. Our implementation of the proposed method in MATLAB takes approximately 0.7 sec on a 4^{th} generation 3.6 GHz Intel Core i7 to estimate the 2D displacement fields of size 1000×100 for an image of the same size. Faster performance can be achieved by using an implementation in MATLAB MEX functions.

In all simulation and phantom experiments, the tunable parameters of the GLUE algorithm are set to $\alpha_1 = 5$, $\alpha_2 = 1$, $\beta_1 = 5$, $\beta_2 = 1$, the tunable parameter of the DP [49] is $\alpha_{DP} = 0.2$. In the in-vivo ablation experiments, α_1 and β_1 are increased to 20 due to the high level of noise in the RF data. The tunable parameters of the DPAM algorithm are always set to $\alpha = 5$, $\beta_a = 10$, $\beta_l = 0.005$ and T = 0.2 [1]. Ultrasound machines have pre-settings for imaging different organs and applications, and the elastography parameters can

TABLE I
THE SNR AND CNR VALUES OF THE SIMULATION EXPERIMENT. TARGET WINDOWS (5MM X 5MM) AND BACKGROUND WINDOWS (3MM X 3MM) USED FOR CNR CALCULATION ARE SHOWN IN FIGURE 2. THE SNR IS CALCULATED IN THE BACKGROUND WINDOW. MAXIMUM VALUES ARE IN BOLD FONT.

	SNR		CNR	
Experiment 1	Axial	Lateral	Axial	Lateral
NCC	2.14	0.52	4.94	7.69
DPAM	5.29	4.50	14.62	10.87
GLUE	**44.63**	**4.61**	**26.31**	**11.03**

TABLE II
THE SNR AND CNR VALUES OF THE SIMULATION EXPERIMENT. TARGET WINDOWS (5MM X 5MM) AND BACKGROUND WINDOWS (3MM X 3MM) USED FOR CNR CALCULATION ARE SHOWN IN FIGURE 3. THE SNR IS CALCULATED IN THE BACKGROUND WINDOW.

	SNR		CNR	
Experiment 2	Axial	Lateral	Axial	Lateral
NCC	Fails	Fails	Fails	Fails
DPAM	Fails	Fails	Fails	Fails
GLUE	43.70	4.41	17.45	6.72

also be tuned based on the application. The desired parameters for a new application (breast, thyroid, prostate, etc.) can be obtained by visually inspecting the displacement map: if the map is too noisy or too smooth, the regularization weight should be respectively increased or decreased.

Estimation of lateral displacement is significantly more difficult mainly due to the poor resolution of ultrasound images in this direction, thereby limiting most of the previous work to only calculate axial strain images. Simultaneous estimation of the displacement filed for the entire image, however, allows us to substantially improve the quality of both axial and lateral displacements. Therefore, we calculate both axial and lateral strains in simulation and phantom experiments. The unitless metrics signal to noise ratio (SNR) and contrast to noise ratio (CNR) are used to quantitatively compare the results [2]:

$$\mathrm{CNR} = \frac{C}{N} = \sqrt{\frac{2(\bar{s_b} - \bar{s_t})^2}{\sigma_b^2 + \sigma_t^2}},\ \mathrm{SNR} = \frac{\bar{s}}{\sigma} \qquad (14)$$

where $\bar{s_t}$ and $\bar{s_b}$ are the spatial strain average of the target and background, σ_t^2 and σ_b^2 are the spatial strain variance of the target and background, and $\bar{s}$ and σ are the spatial average and variance of a window in the strain image respectively. The SNR and CNR are calculated for the results using small windows which are located in approximately uniform regions, and therefore, strain is expected to be relatively constant within each window.

A. Simulation Results

Field II software [58] is used to simulate ultrasound images, and ABAQUS (Providence, RI) software is used to estimate deformations in a digital phantom using finite element method (FEM). The displacement and strain fields are then calculated from the simulated ultrasound images using DPAM and GLUE. For the purposes of comparison, strain images were also calculated using a standard cross correlation method with 80% overlap and a nine point 2D parabolic interpolation to find the 2D sub-sample location of the correlation peak. Figure 2 shows the results of the first simulation experiment. The axial and lateral strains are depicted in (a) to (d), and (e) to (h) respectively. (a) and (e) are the ground truth axial and lateral strain images simulated using FEM. The axial strain images obtained by cross correlation, DPAM and GLUE are shown in (b), (c) and (d), respectively. The second row shows the corresponding lateral strains. It is clear that GLUE significantly outperforms DPAM and NCC in both reducing noise and improving contrast.

In the second simulation (Figure 3), we consider tissue slippage which might happen in real world, e.g. at the boundary of different organs such as prostate and rectum [59] or for lesions that are not connected to the surrounding tissue. In this experiment, the ultrasound image related to pre-compression is the same as before, whereas a vertical slippage occurs in the second image. The average axial strains to the left and right of the slippage line are respectively 1% and 2%. The strain images generated using cross correlation, DPAM and GLUE are depicted in (b), (c) and (d) for axial strain and (f), (g) and (h) for lateral strain respectively. As one can see, NCC and DPAM fail in this situation while GLUE accurately computes TDE despite the large discontinuity in the underlying deformation field.

The corresponding SNR and CNR values are measured for both simulation experiments. CNR values are calculated between the target (tumor) and background (outside the target) windows each of size 5 mm $\times$ 5 mm and 3 mm $\times$ 3 mm respectively, and are provided in Table I and Table II. SNR values are also shown in the table, which are calculated for the background windows. GLUE provides substantially higher SNR and CNR values compared to both NCC and DPAM.

TABLE III
THE SNR AND CNR OF THE STRAIN IMAGES OF THE EXPERIMENTAL PHANTOM. TARGET AND BACKGROUND WINDOWS USED FOR CNR CALCULATION ARE SHOWN IN FIGURE 4. THE SNR IS CALCULATED FOR THE BACKGROUND WINDOW. MAXIMUM VALUES ARE IN BOLD FONT.

	SNR		CNR	
	Axial	Lateral	Axial	Lateral
NCC	2.20	3.60	1.07	0.39
DPAM	26.21	4.77	16.01	3.25
GLUE	**29.85**	**7.22**	**18.21**	**4.09**

B. Phantom Results

For experimental evaluation, RF data is acquired from a CIRS elastography phantom (Norfolk, VA) using an Antares Siemens system (Issaquah, WA) at the center frequency of 6.67 MHz with a VF10-5 linear array at a sampling rate of 40 MHz. The results of NCC, DPAM and GLUE methods are shown in Figure 4, along with the target and background windows used for SNR and CNR calculation. SNR is only calculated for the background window. The results are summarized in Table III. Again, GLUE substantially improves both SNR and CNR in both axial and lateral strain images.

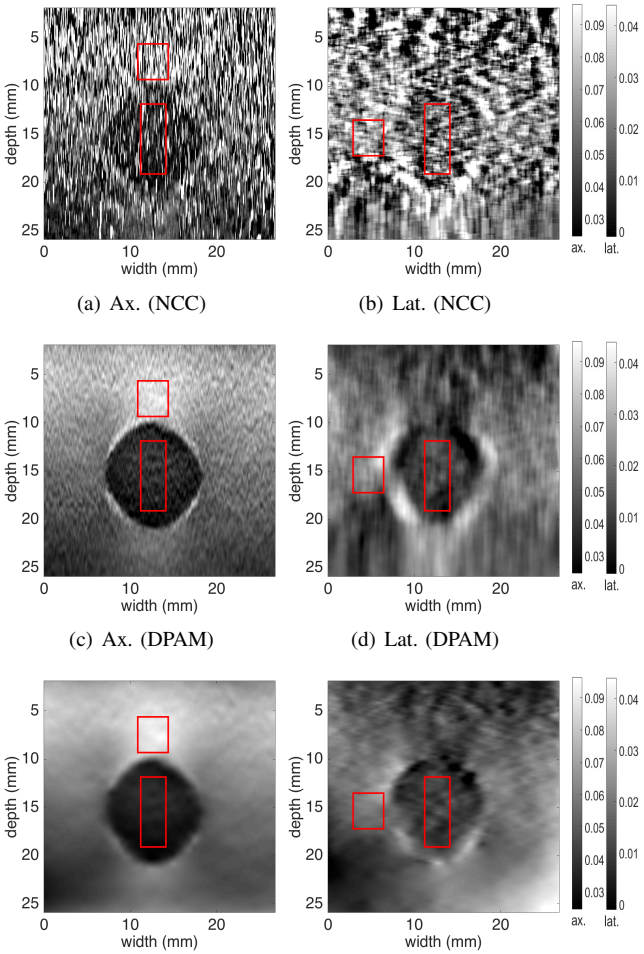

(a) Ax. (NCC) (b) Lat. (NCC)

(c) Ax. (DPAM) (d) Lat. (DPAM)

(e) Ax. (GLUE) (f) Lat. (GLUE)

Fig. 4. Results of the phantom experiment. Axial and lateral strain images as well as the target and background windows (in red) for calculation of SNR and CNR are shown (see Table III for results). The hard lesion is spherical and has a diameter of 1 cm. The axial and lateral strain scales are identical for NCC, DPAM and GLUE to ease comparison, and are shown in the right column.

C. In-vivo Results

The *In-vivo* data is acquired from four patients undergoing open surgical radiofrequency thermal ablation for primary or secondary liver cancers. This data is collected as follows at Johns Hopkins Hospital: for the first patient, ultrasound RF data is acquired only after ablation. For the second, third, and fourth patients, ultrasound RF data is collected both before and after ablation. Data collection from the tumour involved holding the probe is hard-to-reach locations and angles, which lead to unwanted out-of-plane motions of the probe. In addition, microbubbles and high temperature gradients created by the ablation process add noise in the the RF data. Furthermore, the pulsation of hepatic vessels create complicated deformation fields. Therefore, the pre- and post-compression images suffer from high levels of decorrelation. Traditional NCC failed to estimate the displacement field, and therefore, we only show GLUE and DPAM results in this data.

Figure 5 shows B-mode scans, strain images and computed tomography (CT) scans obtained after RF ablation in all four patients. Note that the extent of the ablation is almost completely invisible in B-mode images. The coagulated tissue is clearly visible in strain images, and is marked with red arrows. The CNR values of the ablation lesion are calculated between the target (inside the ablation lesion) and background (outside the target) windows, each of size 6 mm $\times$ 6 mm. The SNR values are calculated for the background windows. Table IV shows that we obtain approximately 5-fold and 4-fold improvements in SNR and CNR respectively by utilizing GLUE method instead of DPAM. The ablation lesion in strain images corresponds well to the post-operative CT images shown in the right column.

Figure 6 and 7 show pre-ablation results obtained by DPAM and GLUE in second, third and fourth patients. In Figure 6, the tumors are marked with red arrows, and are hardly visible in the B-mode images in (a) and (d). The strain images provide a significantly improved contrast between the tumor and healthy tissue. CNR values are calculated between target (inside the tumor) and background (outside the target) windows, each of size 6 mm $\times$ 6 mm. The SNR values are calculated for the background windows (Table V). Again, we see large improvements with GLUE as a result of utilizing all the data in the RF frames.

Figure 7 shows the B-mode, strain, and CT images of Patient 4. All images are obtained before ablation. In (a), the tumor is not visible in the B-mode image. A and B are veins which compress easily due to their low pressure. In contrast, C, D (Arteries) and E (middle hepatic vein) pulsate with the heart beat and may have low or high pressure. The probe motion and variations in the diameter is shown in graph (d). Two ultrasound images US 1 and US 2 (see part (d)) are obtained while the vein diameter variation and probe motion

TABLE IV
THE SNR AND CNR VALUES OF THE STRAIN IMAGES OF THE *in-vivo* DATA IN FIGURE 5. THE SNR IS CALCULATED FOR THE BACKGROUND WINDOW OF SIZE 6 MM $\times$ 6 MM. MAXIMUM VALUES ARE IN BOLD FONT.

	SNR		CNR	
	DPAM	GLUE	DPAM	GLUE
P1	7.94	**56.21**	3.73	**13.64**
P2	3.34	**13.04**	1.46	**12.42**
P3	4.47	**23.29**	5.45	**20.14**
P4	3.22	**10.11**	3.60	**6.62**
average	4.74	**25.66**	3.56	**13.20**
improv. %	-	441	-	271

TABLE V
THE SNR AND CNR OF THE STRAIN IMAGES OF THE *in-vivo* DATA IN FIGURES 6 AND 7. THE CNR CALCULATED FOR THE TARGET AND BACKGROUND WINDOW EACH OF SIZE 6MM $\times$ 6MM. THE SNR IS CALCULATED FOR THE BACKGROUND WINDOW. MAXIMUM VALUES ARE IN BOLD FONT.

	SNR		CNR	
	DPAM	GLUE	DPAM	GLUE
P2	12.52	**17.71**	11.27	**13.72**
P3	8.39	**30.15**	4.32	**12.92**
P4 (US 1&2)	16.68	**23.23**	2.19	**13.29**
P4 (US 3&4)	9.97	**26.21**	1.38	**14.03**
average	11.89	**24.32**	4.79	**13.49**
improv. %	-	105	-	182

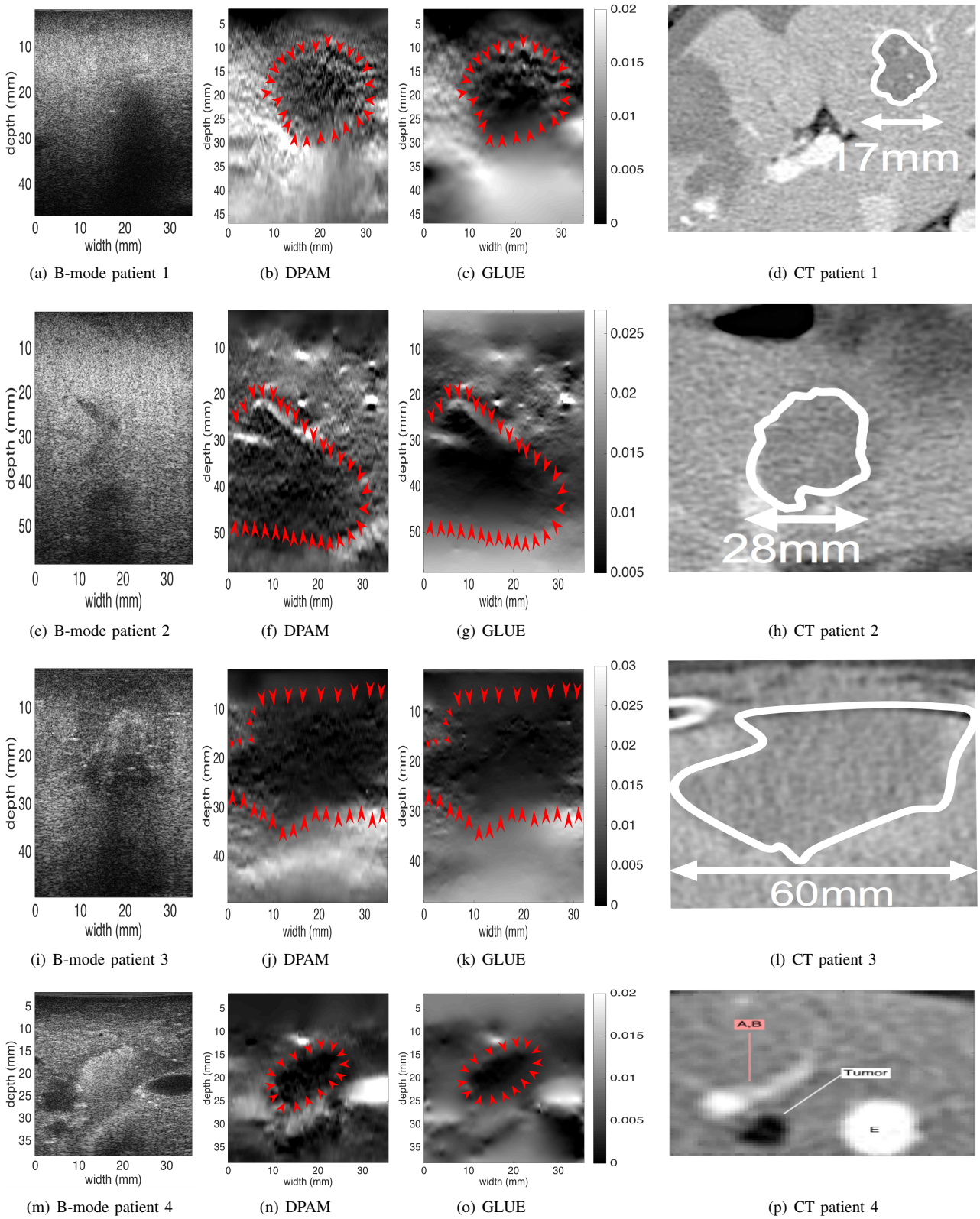

(a) B-mode patient 1 (b) DPAM (c) GLUE (d) CT patient 1

(e) B-mode patient 2 (f) DPAM (g) GLUE (h) CT patient 2

(i) B-mode patient 3 (j) DPAM (k) GLUE (l) CT patient 3

(m) B-mode patient 4 (n) DPAM (o) GLUE (p) CT patient 4

Fig. 5. *In-vivo* images of the ablation lesion acquired after ablation of liver tumours. Each row corresponds to one patient. The first column shows ultrasound images, and the second and third columns respectively show the results of DPAM and GLUE. The ablation lesion is marked with red arrows, and is clearly visible in strain images. CT images with the delineated ablation lesions are shown in the right column.

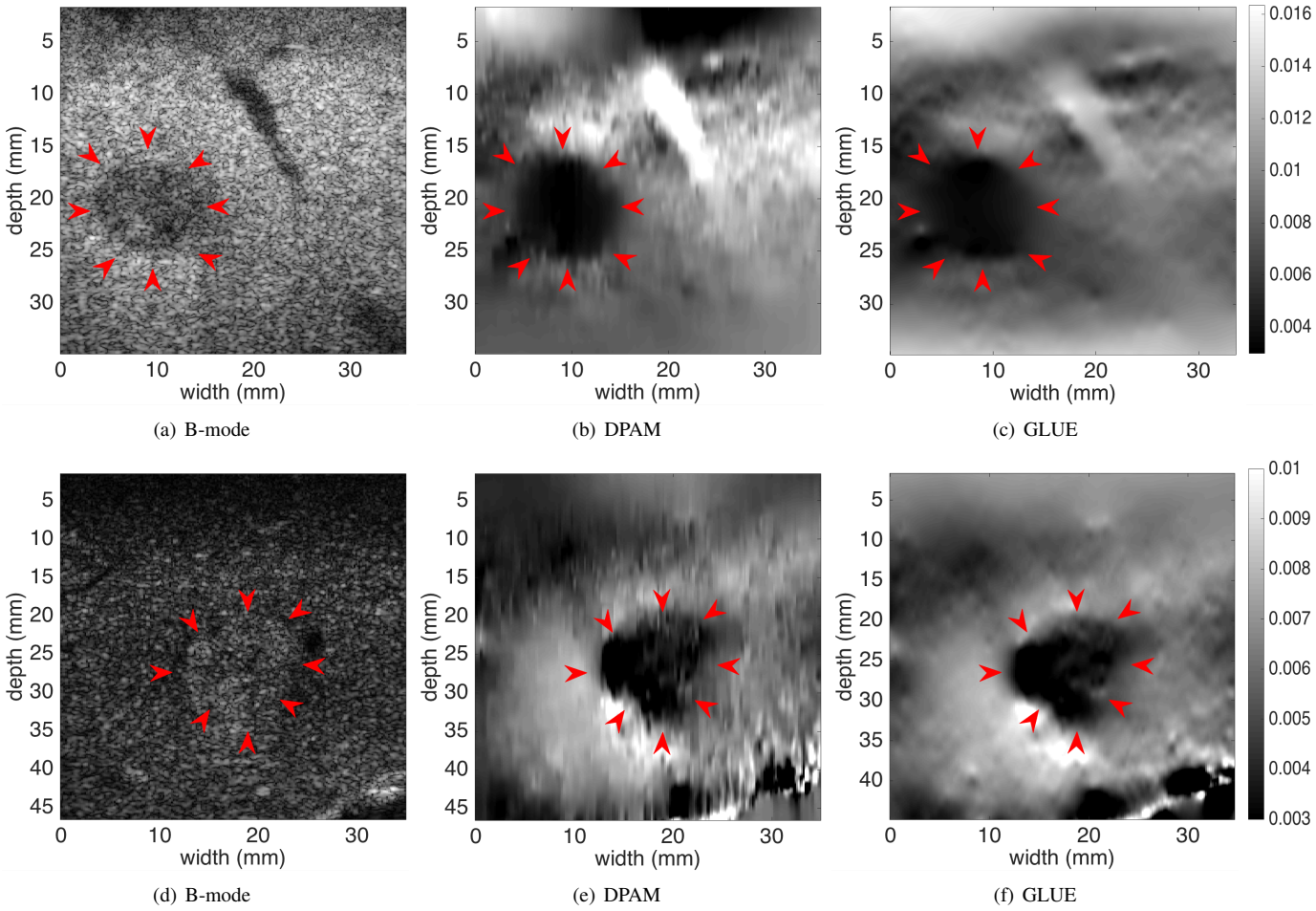

(a) B-mode (b) DPAM (c) GLUE

(d) B-mode (e) DPAM (f) GLUE

Fig. 6. B-mode and strain images of the patient data before ablation. First and second rows respectively correspond to patients 2 and 3. The red arrows point to the tumours. The strain images provide a substantially improved visualization of the tumours compared to the B-mode ultrasound images.

are in the same direction due to high blood pressure. Another pair of ultrasound images, US 3 and US 4, are acquired at low blood pressure when they are pointing to the opposite side in graph (d). Thus, we acquired two paired ultrasound frames at two different phases of the heart beat. The result of DPAM and GLUE using US 1 and 2 are shown in (b) and (e) respectively. US 3 and US 4 are used to obtain DPAM and GLUE strain images in (c) and (f). It is very interesting to compare the middle hepatic vein (marked as E in (a)) in strain images in the second and third columns: E looks hard in the second column, and soft in the third column. The reason lies in large pulsation of the middle hepatic vein due to heart beats. CT scans corresponding to two different phases of the heart beat are depicted in (g) and (h). Here, A to D mark the same anatomy as (a).

Table V summarizes the SNR and CNR values of patients 2 to 4. Average values for DPAM and GLUE are shown in the fifth row. GLUE outperforms DPAM by approximately 2-fold and 3-fold improvements in SNR and CNR values.

IV. Discussion

Incorporating the prior information of displacement continuity generally improves the TDE. Window-based methods enforce continuity in a small window, DPAM utilizes continuity in a single RF-line, and GLUE utilizes displacement continuity throughout the image. This is a reason for the improvement from window-based methods to DPAM to GLUE. However, there is also a disadvantage of using prior information, which is rooted in the bias-variance trade-off [60], [61]. The prior information decreases the variance, but it increases the bias. The increase in the bias can lead to strain images with lower contrast. Nevertheless, the substantial improvement in the CNR shows that GLUE strikes a balance between bias and variance.

In order to image some of the tumors during the intervention, the ultrasound probe had to be held at difficult angles, which lead to unwanted out-of-plane motion of the probe during the palpation. Furthermore, ablation creates microbubbles and high temperature gradients, which add high levels of noise to the RF data. Therefore, the pre- and post-compression images suffer from high decorrelation. An advantage of DPAM and GLUE lies within the simultaneous displacement estimation of several samples and exploitation of the continuity prior. As such, both of these methods generate displacement fields from such noisy data, whereas traditional window-based methods calculate the displacement of each

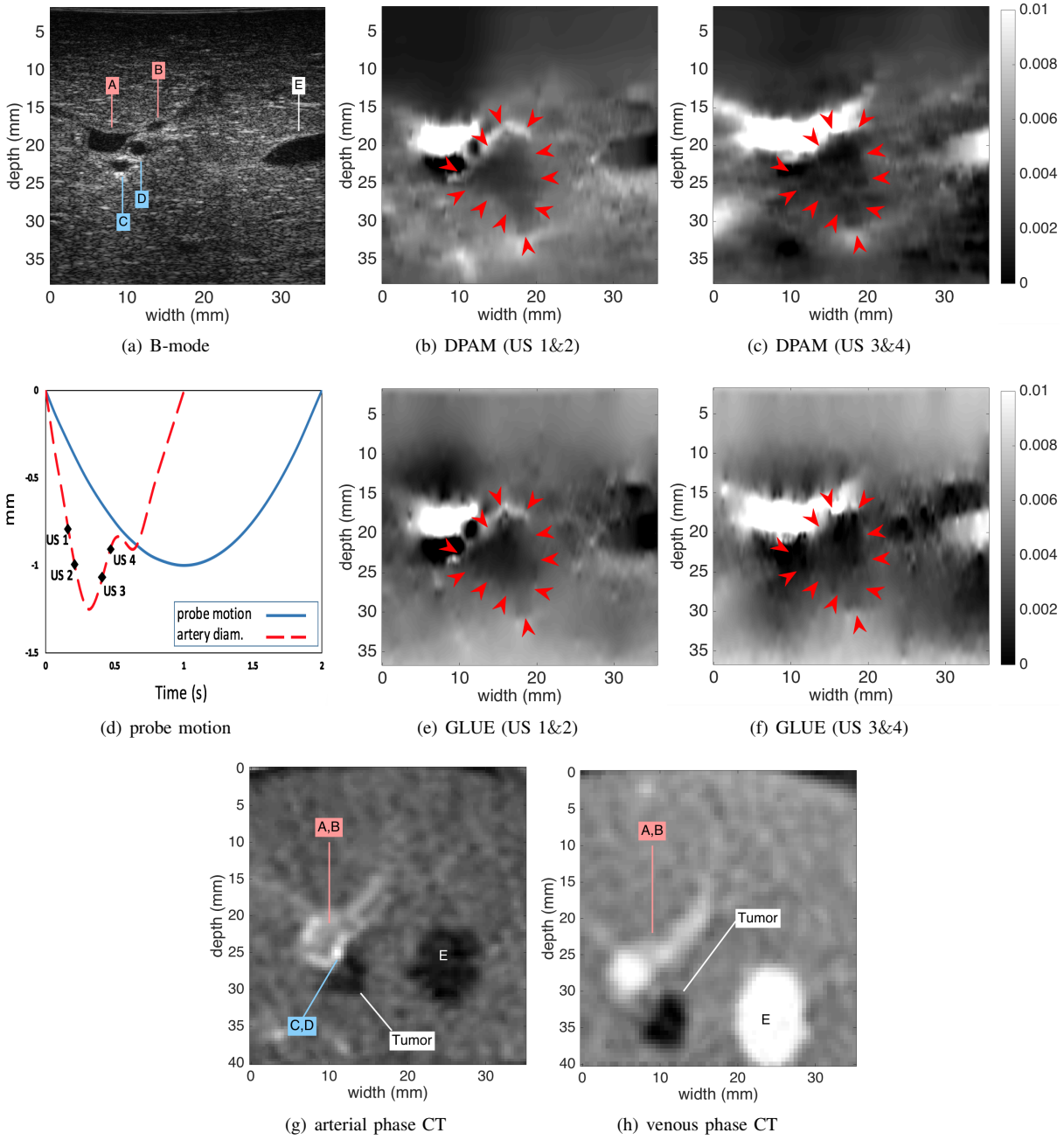

(a) B-mode (b) DPAM (US 1&2) (c) DPAM (US 3&4)

(d) probe motion (e) GLUE (US 1&2) (f) GLUE (US 3&4)

(g) arterial phase CT (h) venous phase CT

Fig. 7. B-mode and strain images of patient 4 before ablation. (a) shows B-mode image, and (b) and (c) show the strain images from the DPAM method using US 1 and 2 frames (for b) and US 3 and 4 frames (for c). (d) shows the motion of the probe and the variation in the diameter of the arteries due to the heart beat. (e) and (f) show results of the GLUE method. (g) is the arterial phase and (h) is the venous phase contrast CT images. The tumor is marked with red arrows in (b), (c), (e), and (f).

window independently and can fail for decorrelated windows. An example of the output of the traditional NCC-based TDE method on this liver data is shown in [46].

The regularization term in the GLUE cost function enforces displacement continuity. The strain field is the spatial derivative of the displacement field, and as such, is piecewise continuous in theory (i.e. strain can be discontinuous). This is in fact desired since the strain field can be discontinuous in the boundary between two different types of tissue. In practice, however, large kernels are commonly used for performing the spatial gradient operation to alleviate noise amplification of the derivative operator. This large kernel guarantees smooth strain fields, but has the disadvantage of blurring the boundary of two different types of tissue. We have proposed Kalman filter [1] and bilateral filter [62] to generate piecewise continuous strain fields that are sharp at the boundary of two different tissue types but are smooth within each type of tissue.

V. Conclusion

In this paper, we introduced GLUE, a novel technique for calculating both axial and lateral displacement fields between two frames of RF data. We estimated the displacement field of the entire image simultaneously, which led to substantial improvement over previous work. An unoptimized implementation of the proposed method in MATLAB takes only 0.7 sec on a typical CPU. Therefore, our technique is highly suitable for implementation in commercial ultrasound systems. An implementation of GLUE is publicly available from the website of the corresponding author.

Acknowledgements

This work was supported by the Richard and Edith Strauss Canada Foundation. The *in-vivo* data was collected at Johns Hopkins Hospital. We would like to thank the principal investigators Drs. E. Boctor, M. Choti and G. Hager who provided us with the data. The authors would also like to thank R. Shams, M. Derakhshan and H. Khodadadi for valuable discussions, and anonymous reviewers for their constructive feedback.

References

[1] H. Rivaz, E. M. Boctor, M. A. Choti, and G. D. Hager, "Real-time regularized ultrasound elastography," *Medical Imaging, IEEE Transactions on*, vol. 30, no. 4, pp. 928–945, 2011.

[2] J. Ophir, S. Alam, B. Garra, F. Kallel, E. Konofagou, T. Krouskop, and T. Varghese, "Elastography: ultrasonic estimation and imaging of the elastic properties of tissues," *Proceedings of the Institution of Mechanical Engineers, Part H: Journal of Engineering in Medicine*, vol. 213, no. 3, pp. 203–233, 1999.

[3] T. J. Hall, P. Barbone, A. A. Oberai, J. Jiang, J. F. Dord, S. Goenezen, and T. G. Fisher, "Recent results in nonlinear strain and modulus imaging," *Current medical imaging reviews*, vol. 7, no. 4, p. 313, 2011.

[4] G. Treece, J. Lindop, L. Chen, J. Housden, R. Prager, and A. Gee, "Real-time quasi-static ultrasound elastography," *Interface focus*, pp. 1–13, 2011.

[5] K. Parker, M. Doyley, and D. Rubens, "Corrigendum: Imaging the elastic properties of tissue: the 20 year perspective," *Physics in medicine & biology*, vol. 57, no. 16, pp. 5359–5360, 2012.

[6] J.-L. Gennisson, T. Deffieux, M. Fink, and M. Tanter, "Ultrasound elastography: principles and techniques," *Diagnostic and interventional imaging*, vol. 94, no. 5, pp. 487–495, 2013.

[7] A. Tang, G. Cloutier, N. M. Szeverenyi, and C. B. Sirlin, "Ultrasound elastography and mr elastography for assessing liver fibrosis: Part 1, principles and techniques," *American Journal of Roentgenology*, vol. 205, no. 1, pp. 22–32, 2015.

[8] J. Bercoff, M. Tanter, and M. Fink, "Supersonic shear imaging: a new technique for soft tissue elasticity mapping," *IEEE transactions on ultrasonics, ferroelectrics, and frequency control*, vol. 51, no. 4, pp. 396–409, 2004.

[9] K. Nightingale, M. S. Soo, R. Nightingale, and G. Trahey, "Acoustic radiation force impulse imaging: in vivo demonstration of clinical feasibility," *Ultrasound in medicine & biology*, vol. 28, no. 2, pp. 227–235, 2002.

[10] M. Doyley, "Model-based elastography: a survey of approaches to the inverse elasticity problem," *Physics in medicine and biology*, vol. 57, no. 3, p. R35, 2012.

[11] O. Goksel, H. Eskandari, and S. E. Salcudean, "Mesh adaptation for improving elasticity reconstruction using the fem inverse problem," *IEEE transactions on medical imaging*, vol. 32, no. 2, pp. 408–418, 2013.

[12] C. Hoerig, J. Ghaboussi, M. Fatemi, and M. F. Insana, "A new approach to ultrasonic elasticity imaging," in *SPIE Medical Imaging*. International Society for Optics and Photonics, 2016, pp. 97 900G–97 900G.

[13] O. A. Babaniyi, A. A. Oberai, and P. E. Barbone, "Recovering vector displacement estimates in quasistatic elastography using sparse relaxation of the momentum equation," *Inverse Problems in Science and Engineering*, vol. 25, no. 3, pp. 326–362, 2017.

[14] S. R. Mousavi, A. Sadeghi-Naini, G. J. Czarnota, and A. Samani, "Towards clinical prostate ultrasound elastography using full inversion approach," *Medical physics*, vol. 41, no. 3, 2014.

[15] S. Catheline, F. Wu, and M. Fink, "A solution to diffraction biases in sonoelasticity: the acoustic impulse technique," *The Journal of the Acoustical Society of America*, vol. 105, no. 5, pp. 2941–2950, 1999.

[16] M. Tanter, J. Bercoff, A. Athanasiou, T. Deffieux, J.-L. Gennisson, G. Montaldo, M. Muller, A. Tardivon, and M. Fink, "Quantitative assessment of breast lesion viscoelasticity: initial clinical results using supersonic shear imaging," *Ultrasound in medicine & biology*, vol. 34, no. 9, pp. 1373–1386, 2008.

[17] P. Song, H. Zhao, A. Manduca, M. W. Urban, J. F. Greenleaf, and S. Chen, "Comb-push ultrasound shear elastography (cuse): a novel method for two-dimensional shear elasticity imaging of soft tissues," *IEEE transactions on medical imaging*, vol. 31, no. 9, pp. 1821–1832, 2012.

[18] J. Ophir, I. Cespedes, H. Ponnekanti, Y. Yazdi, and X. Li, "Elastography: a quantitative method for imaging the elasticity of biological tissues," *Ultrasonic imaging*, vol. 13, no. 2, pp. 111–134, 1991.

[19] K. M. Hiltawsky, M. Krüger, C. Starke, L. Heuser, H. Ermert, and A. Jensen, "Freehand ultrasound elastography of breast lesions: clinical results," *Ultrasound in medicine & biology*, vol. 27, no. 11, pp. 1461–1469, 2001.

[20] M. M. Doyley, J. C. Bamber, F. Fuechsel, and N. L. Bush, "A freehand elastographic imaging approach for clinical breast imaging: system development and performance evaluation," *Ultrasound in medicine & biology*, vol. 27, no. 10, pp. 1347–1357, 2001.

[21] M. Yamakawa, N. Nitta, T. Shiina, T. Matsumura, S. Tamano, T. Mitake, and E. Ueno, "High-speed freehand tissue elasticity imaging for breast diagnosis," *Japanese journal of applied physics*, vol. 42, no. 5S, p. 3265, 2003.

[22] T. J. Hall, Y. Zhu, and C. S. Spalding, "In vivo real-time freehand palpation imaging," *Ultrasound in medicine & biology*, vol. 29, no. 3, pp. 427–435, 2003.

[23] J. E. Lindop, G. M. Treece, A. H. Gee, and R. W. Prager, "3d elastography using freehand ultrasound," *Ultrasound in medicine & biology*, vol. 32, no. 4, pp. 529–545, 2006.

[24] R. Zahiri and S. Salcudean, "Motion estimation in ultrasound images using time domain cross correlation with prior estimates," *IEEE Trans. Biomed. Eng.*, vol. 53, no. 10, pp. 1990–2000, Oct. 2006.

[25] R. G. Lopata, M. M. Nillesen, H. H. Hansen, I. H. Gerrits, J. M. Thijssen, and C. L. De Korte, "Performance evaluation of methods for two-dimensional displacement and strain estimation using ultrasound radio frequency data," *Ultrasound in medicine & biology*, vol. 35, no. 5, pp. 796–812, 2009.

[26] A. Nahiyan and M. K. Hasan, "Hybrid algorithm for elastography to visualize both solid and fluid-filled lesions," *Ultrasound in medicine & biology*, vol. 41, no. 4, pp. 1058–1078, 2015.

[27] X. Pan, K. Liu, J. Shao, J. Gao, L. Huang, J. Bai, and J. Luo, "Performance comparison of rigid and affine models for motion estimation using ultrasound radio-frequency signals," *IEEE transactions on ultrasonics, ferroelectrics, and frequency control*, vol. 62, no. 11, pp. 1928–1943, 2015.

[28] M. O'Donnell, A. R. Skovoroda, B. M. Shapo, and S. Y. Emelianov, "Internal displacement and strain imaging using ultrasonic speckle tracking," *IEEE transactions on ultrasonics, ferroelectrics, and frequency control*, vol. 41, no. 3, pp. 314–325, 1994.

[29] X. Chen, M. J. Zohdy, S. Y. Emelianov, and M. O'Donnell, "Lateral speckle tracking using synthetic lateral phase," *IEEE transactions on ultrasonics, ferroelectrics, and frequency control*, vol. 51, no. 5, pp. 540–550, 2004.

[30] J. E. Lindop, G. M. Treece, A. H. Gee, and R. W. Prager, "Phase-based ultrasonic deformation estimation," *Ultrasonics, Ferroelectrics, and Frequency Control, IEEE Transactions on*, vol. 55, no. 1, pp. 94–111, 2008.

[31] S. Ara, F. Mohsin, F. Alam, S. A. Rupa, S. Y. Lee, M. K. Hasan, and R. Awwal, "Phase-based direct average strain estimation for elastography," *IEEE transactions on ultrasonics, ferroelectrics, and frequency control*, vol. 60, no. 11, pp. 2266–2283, 2013.

[32] L. Yuan and P. C. Pedersen, "Analytical phase-tracking-based strain estimation for ultrasound elasticity," *IEEE transactions on ultrasonics, ferroelectrics, and frequency control*, vol. 62, no. 1, pp. 185–207, 2015.

[33] A. Pesavento, C. Perrey, M. Krueger, and H. Ermert, "A time-efficient and accurate strain estimation concept for ultrasonic elastography using iterative phase zero estimation," *IEEE transactions on ultrasonics, ferroelectrics, and frequency control*, vol. 46, no. 5, pp. 1057–1067, 1999.

[34] R. Dickinson and C. Hill, "Measurement of soft tissue motion using correlation between a-scans," *Ultrasound in medicine & biology*, vol. 8, no. 3, pp. 263–271, 1982.
[35] M. Bilgen and M. F. Insana, "Deformation models and correlation analysis in elastography," *The journal of the acoustical society of America*, vol. 99, no. 5, pp. 3212–3224, 1996.
[36] B. H. Friemel, L. N. Bohs, and G. E. Trahey, "Relative performance of two-dimensional speckle-tracking techniques: normalized correlation, non-normalized correlation and sum-absolute-difference," in *Ultrasonics Symposium, 1995. Proceedings., 1995 IEEE*, vol. 2. IEEE, 1995, pp. 1481–1484.
[37] E. Konofagou and J. Ophir, "A new elastographic method for estimation and imaging of lateral displacements, lateral strains, corrected axial strains and poissonâĂŹs ratios in tissues," *Ultrasound in medicine & biology*, vol. 24, no. 8, pp. 1183–1199, 1998.
[38] E. S. Ebbini, "Phase-coupled two-dimensional speckle tracking algorithm," *IEEE transactions on ultrasonics, ferroelectrics, and frequency control*, vol. 53, no. 5, pp. 972–990, 2006.
[39] G. M. Treece, J. E. Lindop, A. H. Gee, and R. W. Prager, "Freehand ultrasound elastography with a 3-d probe," *Ultrasound in medicine & biology*, vol. 34, no. 3, pp. 463–474, 2008.
[40] J. Jiang and T. J. Hall, "A coupled subsample displacement estimation method for ultrasound-based strain elastography," *Physics in medicine and biology*, vol. 60, no. 21, p. 8347, 2015.
[41] H. Chen, H. Shi, and T. Varghese, "Improvement of elastographic displacement estimation using a two-step cross-correlation method," *Ultrasound in medicine & biology*, vol. 33, no. 1, pp. 48–56, 2007.
[42] J. Grondin, E. Wan, A. Gambhir, H. Garan, and E. E. Konofagou, "Intracardiac myocardial elastography in canines and humans in vivo," *IEEE transactions on ultrasonics, ferroelectrics, and frequency control*, vol. 62, no. 2, pp. 337–349, 2015.
[43] S. K. Alam and J. Ophir, "Reduction of signal decorrelation from mechanical compression of tissues by temporal stretching: Applications to elastography," *Ultrasound in medicine & biology*, vol. 23, no. 1, pp. 95–105, 1997.
[44] S. K. Alam, J. Ophir, and E. E. Konofagou, "An adaptive strain estimator for elastography," *IEEE transactions on ultrasonics, ferroelectrics, and frequency control*, vol. 45, no. 2, pp. 461–472, 1998.
[45] P. Chaturvedi, M. F. Insana, and T. J. Hall, "2-d companding for noise reduction in strain imaging," *IEEE transactions on ultrasonics, ferroelectrics, and frequency control*, vol. 45, no. 1, pp. 179–191, 1998.
[46] A. Kuzmin, A. M. Zakrzewski, B. W. Anthony, and V. Lempitsky, "Multi-frame elastography using a handheld force-controlled ultrasound probe," *IEEE transactions on ultrasonics, ferroelectrics, and frequency control*, vol. 62, no. 8, pp. 1486–1500, 2015.
[47] R. L. Maurice and M. Bertrand, "Lagrangian speckle model and tissue-motion estimation-theory [ultrasonography]," *IEEE transactions on medical imaging*, vol. 18, no. 7, pp. 593–603, 1999.
[48] C. Pellot-Barakat, F. Frouin, M. F. Insana, and A. Herment, "Ultrasound elastography based on multiscale estimations of regularized displacement fields," *Medical Imaging, IEEE Transactions on*, vol. 23, no. 2, pp. 153–163, 2004.
[49] H. Rivaz, E. Boctor, P. Foroughi, R. Zellars, G. Fichtinger, and G. Hager, "Ultrasound elastography: a dynamic programming approach," *Medical Imaging, IEEE Transactions on*, vol. 27, no. 10, pp. 1373–1377, 2008.
[50] E. Brusseau, J. Kybic, J.-F. Déprez, and O. Basset, "2-d locally regularized tissue strain estimation from radio-frequency ultrasound images: Theoretical developments and results on experimental data," *IEEE TMI*, vol. 27, no. 2, pp. 145–160, 2008.
[51] H. Rivaz, E. M. Boctor, M. A. Choti, and G. D. Hager, "Ultrasound elastography using multiple images," *Medical image analysis*, vol. 18, no. 2, pp. 314–329, 2014.
[52] L. Petitclerc, G. Sebastiani, G. Gilbert, G. Cloutier, and A. Tang, "Liver fibrosis: Review of current imaging and mri quantification techniques," *Journal of Magnetic Resonance Imaging*, 2016.
[53] L. H. Thomas, "Elliptic problems in linear difference equations over a network," *Watson Sci. Comput. Lab. Rept., Columbia University, New York*, vol. 1, 1949.
[54] D. M. Young, *Iterative solution of large linear systems*. Elsevier, 1971.
[55] Z. Wen, W. Yin, and Y. Zhang, "Solving a low-rank factorization model for matrix completion by a nonlinear successive over-relaxation algorithm," *Mathematical Programming Computation*, vol. 4, no. 4, pp. 333–361, 2012.
[56] Y.-H. Shao, C.-H. Zhang, X.-B. Wang, and N.-Y. Deng, "Improvements on twin support vector machines," *IEEE transactions on neural networks*, vol. 22, no. 6, pp. 962–968, 2011.
[57] R. Szeliski, *Bayesian modeling of uncertainty in low-level vision*. Springer Science & Business Media, 2012, vol. 79.
[58] J. A. Jensen, "Field: A program for simulating ultrasound systems," in *10th Nordic-Baltic Conference on Biomedical Imaging, Vol. 4, Supplement 1, 351–353*, 1996.
[59] M. S. Hoogeman, M. van Herk, J. de Bois, and J. V. Lebesque, "Strategies to reduce the systematic error due to tumor and rectum motion in radiotherapy of prostate cancer," *Radiotherapy and oncology*, vol. 74, no. 2, pp. 177–185, 2005.
[60] S. Geman, E. Bienenstock, and R. Doursat, "Neural networks and the bias/variance dilemma," *Neural computation*, vol. 4, no. 1, pp. 1–58, 1992.
[61] W. F. Walker and G. E. Trahey, "A fundamental limit on delay estimation using partially correlated speckle signals," *IEEE Transactions on Ultrasonics, Ferroelectrics, and Frequency Control*, vol. 42, no. 2, pp. 301–308, 1995.
[62] H. Khodadadi, A. G. Aghdam, and H. Rivaz, "Edge-preserving ultrasonic strain imaging with uniform precision," in *Engineering in Medicine and Biology Society (EMBC), 2015 37th Annual International Conference of the IEEE*. IEEE, 2015, pp. 3835–3838.

Hoda Sadat Hashemi received her B.Sc. degree in electrical engineering from Sharif University of Technology, Tehran, Iran. She is currently pursuing her M.A.Sc. degree in electrical and computer engineering at Concordia University, Montreal, Canada. Her research interests include medical image processing, ultrasound elastography, computer vision and machine learning.

Hassan Rivaz received his B.Sc. from Sharif University of Technology, his M.A.Sc. from University of British Columbia, and his Ph.D. from Johns Hopkins University. He did a post-doctoral training at McGill University.

He is now an Assistant Professor and a Petro-Canada Young Innovator at the Department of Electrical and Computer Engineering and the PERFORM Centre at Concordia University, where he is directing the IMage Processing And Characterization of Tissue (IMPACT) Lab. He is an Associate Editor of IEEE Trans. on Medical Imaging and an Area Chair of MICCAI 2017. His main research interests are medical image processing, ultrasound elastography, ultrasound imaging, registration, segmentation and machine learning. Clinical applications of his work are in neurosurgery, liver surgery, breast and prostate radiotherapy and musculoskeletal imaging.